

# Bonding between $\pi$ -Conjugated Polycations and Monolayer Graphene: Decisive Role of Anions

Steffen M. Brülls, Valentina Cantatore, Pui Lam Tam, Per Malmberg, Elisabet Ahlberg, Itai Panas, Siegfried Eigler, and Jerker Mårtensson\*



Cite This: *J. Phys. Chem. C* 2023, 127, 1917–1928



Read Online

ACCESS |



Metrics & More



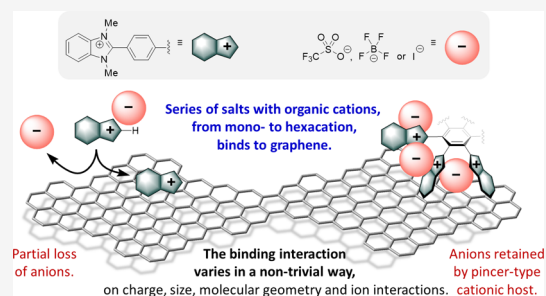
Article Recommendations



Supporting Information

**ABSTRACT:** Functionalization and precise modulation of the electronic properties of graphene are key processes in the development of new applications of this promising material. This study examines the potential of using organic polycations as p-dopants and/or anchoring motifs for non-covalent functionalization. A library of hybrid materials was prepared through wet-chemical non-covalent functionalization. Both chemical vapor deposition graphene and reduced graphene oxide were functionalized with a series of neutral and polycationic benzimidazole-based systems. We report on how both the number of anions and the size, shape, and magnitude of the positive charge of the benzimidazole-based systems cooperatively affect the redox properties as well as the affinity for and the nature of bonding to graphene.

The redox properties of the benzimidazole-based systems were studied by cyclic voltammetry. The functionalized graphene materials were characterized by Raman spectroscopy, X-ray photoelectron spectroscopy, and time-of-flight secondary ion mass spectrometry. Density functional theory calculations were performed to make contact between the experimental results obtained for molecular samples and hybrid materials. No universal dependence of the binding affinity on a single parameter, such as the amount of positive charge or the size of the system, was found. Instead, the cooperative effect of the three-dimensional structure of the benzimidazole-based systems and the number of anions was found to play a pivotal role. Together, these parameters determine the degree of partial electron sharing and magnitude of dispersion forces involved in the binding of members of this family of benzimidazole-based systems to graphene.



## INTRODUCTION

Graphene is the most studied two-dimensional material (2DM).<sup>1–3</sup> All carbon atoms in its crystal lattice are  $sp^2$ -hybridized and arranged in a honeycomb-like structure. Several graphene layers held together by weak dispersion forces on top of each other in an AB sequence form graphite,<sup>4</sup> with an interlayer distance of 3.35 Å.<sup>5</sup> Similarly, graphene can interact with small molecules to form new 2DMs via van der Waals forces, electrostatic interactions, and other forces.<sup>6</sup>

One important consequence of the non-covalent interactions with small molecules is that they can have a doping effect on graphene. This is significant because doping is key to realize the full potential of these graphene-based 2DMs. Electrostatic force microscopy has been used to demonstrate that electron-rich molecules decrease the surface potential of graphene (n-doping) and electron-poor molecules increase the surface potential (p-doping).<sup>7</sup> The doping effect has also been probed by Raman spectroscopy. Characteristic shifts are observed for the graphene-related G and 2D peaks in the Raman spectra as a response to the interaction between graphene and electron-donating or electron-withdrawing molecules.<sup>8</sup> Chemical modifications or functionalization of

graphene with small molecules can also bring other advantages, such as increased stability and catalytic and sensing properties.<sup>6</sup>

The mechanisms of non-covalent interactions between graphene and small molecules, and how they affect the properties of 2DMs, have been recently reviewed.<sup>9</sup> The interaction between graphene and aromatic molecules has been studied computationally. For example, it has been found that the binding energy is mostly governed by dispersive interactions at a large distance.<sup>10</sup> At equilibrium bonding distance, on the other hand, other forces such as electrostatic interactions may make substantial contributions alongside the dispersion interaction. It has also been shown that cations and anions produce more stable complexes with graphene than radical or closed shell molecules of the same structure.<sup>11</sup>

Despite the fact that the field of organic hybrid electronics is growing,<sup>12</sup> the influence and interplay between different

**Received:** October 31, 2022

**Revised:** January 4, 2023

**Published:** January 20, 2023



structural parameters on the non-covalent functionalization are still not fully developed.

Recently, our group reported on the non-covalent functionalization of both graphene prepared by chemical vapor deposition (CVD)<sup>13</sup> and reduced graphene oxide (r-oxo-G)<sup>14,15</sup> with the organic triflate (TfO<sup>-</sup>) salt [Me<sub>6</sub>3][TfO]<sub>3</sub> of the trication 1,3,5-tris(1,3-dimethylbenzimidazolium-2-yl) benzene Me<sub>6</sub>3<sup>3+</sup> (Figure 1).<sup>16</sup> The p-doping effect of the

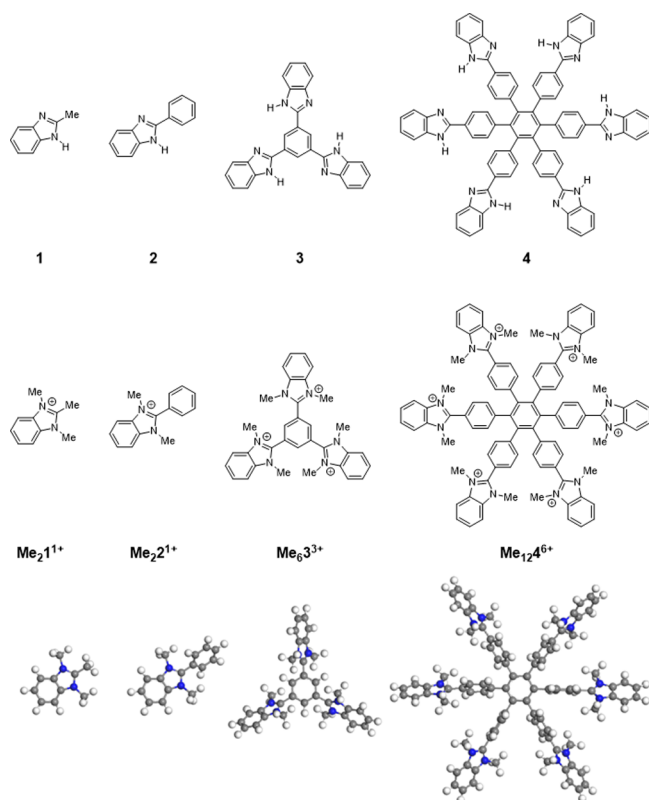


**Figure 1.** Neutral and cationic compounds studied in this work. The Lewis structures of the monocations Me<sub>2</sub>1<sup>+</sup> and Me<sub>2</sub>2<sup>+</sup>, trication Me<sub>6</sub>3<sup>3+</sup>, and hexacation Me<sub>12</sub>4<sup>6+</sup> are shown together with their optimized structures (PBE,<sup>19</sup> GGA functional/CASTEP basis set within the Material Studios framework).

tricationic molecule on the underlying graphene was confirmed in fabricated monolayer graphene/hybrid field-effect transistor devices. This is particularly interesting because dimers of 1,3-dialkyl-2-aryl-2,3-dihydrobenzimidazole, yielding the corresponding pair of 1,3-dialkyl-2-arylbenzimidazolium cations when oxidized, have been applied as effective n-dopants for C<sub>60</sub> and other organic materials.<sup>17,18</sup> This warranted further studies on benzimidazolium-based polycations as p-dopants.

Density functional theory (DFT) calculations showed that the trication Me<sub>6</sub>3<sup>3+</sup> is propeller-shaped in the gas phase. Geometry optimization of the corresponding dication revealed that addition of one additional electron planarized the system substantially. The later geometry resembles the molecular structure obtained in the modeling of the trication–graphene construct. It also revealed that an interplay between electron sharing and increased dispersion interactions due to molecular flattening strengthens the bonding interaction between graphene and the molecular trication.

Here, we investigate how the size and magnitude of the positive charge of aromatic systems affect the affinity for and

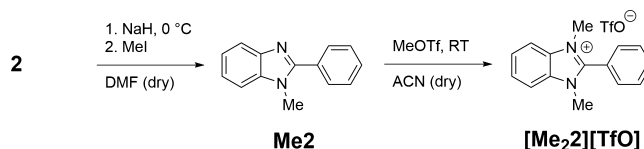
nature of bonding to graphene. The interplay is explored through wet-chemical non-covalent functionalization of CVD graphene and r-oxo-G with a series of benzimidazole-based  $\pi$ -conjugated systems (Figure 1), in conjunction with analysis by cyclic voltammetry, X-ray photoelectron spectroscopy (XPS), and time-of-flight secondary ion mass spectrometry (ToF-SIMS) as well as computational modeling.

The organization of the paper is as follows. First, we describe the synthesis of neutral molecules and ionic compounds used in this study. Next, the wet-chemical methods used to modify the surface of CVD graphene or r-oxo-G with these compounds are detailed. Then, the redox potentials of the neutral molecules and the ionic compounds in solution, recorded by cyclic voltammetry, are discussed, and the connection between the structure of the compounds and electrochemical results is explored using DFT calculations. Computational results for hybrid systems consisting of graphene and various ionic compounds are also presented, with special attention to potential charge transfer. After that, experimental verification of adhesion of the compounds to the graphene surfaces using Raman spectroscopy and imaging mass spectrometry is presented. Finally, XPS data recorded from samples of surface-modified graphene are analyzed in the context of the electrochemical and computational findings.

## METHODS

**Synthesis *N*-Hetero- $\pi$ -Conjugated Systems.** The four sets of two *N*-hetero- $\pi$ -conjugated systems, including two compounds from an earlier study,<sup>16</sup> were obtained by organic synthesis. The synthetic protocols and the characterization of all compounds, shown in Schemes 1 and 2, are detailed in the Supporting Information (Figures S1–S23).

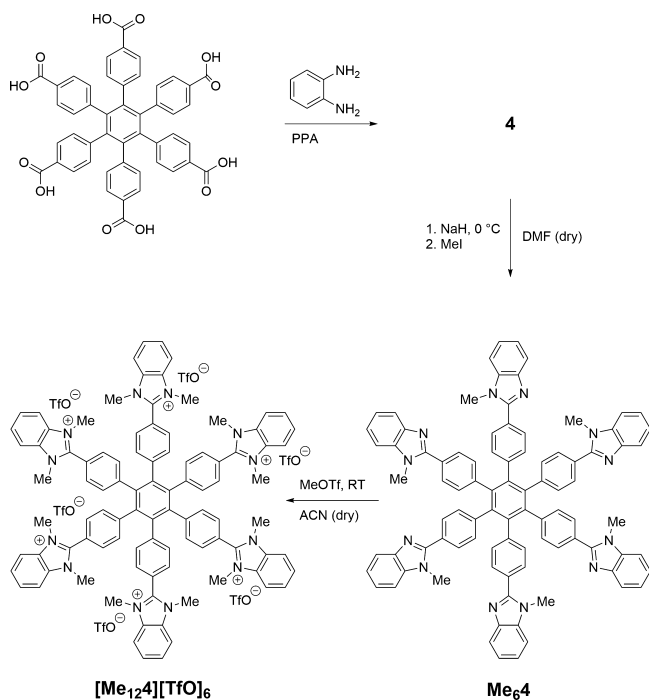
### Scheme 1. Synthesis of Organic Salt [Me<sub>2</sub>2][TfO] from Neutral 2-Phenylbenzimidazole 2 over 1-Methyl-2-phenylbenzimidazole Me2 as the Intermediate Compound



**Electrochemical Characterization.** Cyclic voltammetry was carried out in 0.1 M TBATFB solution in degassed and dry *N,N*-dimethylformamide (DMF) using a three-electrode configuration with glassy carbon as the working electrode and Pt as the counter electrode. The reference electrode was a double junction Ag/Ag<sup>+</sup> electrode, where the inner compartment contained 10 mM AgNO<sub>3</sub> and 0.1 M TBATFB in acetonitrile,  $E = 0.44$  V vs SHE. More experimental information and data are gathered in the Supporting Information (Figures S27–S37).

**2D-Sample Preparation.** CVD graphene and r-oxo-G substrates were incubated in 12 mM methanol solutions of the respective compound for 2 h at 4 °C. Subsequently, the functionalized graphene wafers were removed from the incubation solution and rinsed with methanol to remove excess of compounds. Samples on SiO<sub>2</sub>/Si substrates used for XPS measurements were drop-cast. A 12 mM methanol solution of the selected compound was drop-cast on a blank SiO<sub>2</sub>/Si wafer, and the solvent was allowed to evaporate.

### Scheme 2. Synthesis of the Organic Salt $[\text{Me}_{12}4][\text{TfO}]_6$ from Hexakis(4-carboxyphenyl)benzene via 4



**Surface Analysis.** The modified surfaces of the 2D samples were analyzed by Raman spectroscopy, imaging ToF-SIMS, and XPS. The methods used for surface analysis are described in the Supporting information together with recorded data (Figures S24–S26 and Tables S1–S4).

**Density Functional Theory Modeling.** Computational modeling of molecules and hybrid systems, a supercell comprising a  $12 \times 12$  graphene unit cells and a variety of hexacation complexes, were performed using the Perdew–Burke–Ernzerhof density (PBE)<sup>19</sup> functional within the generalized gradient approximation (GGA). Computational details and results are reported in the Supporting Information.

## RESULTS AND DISCUSSION

**Synthesis.** Four sets of two *N*-hetero- $\pi$ -conjugated systems of varying size and with different amounts of charges were prepared, including two compounds from an earlier study.<sup>16</sup> These sets constitute two series of compounds composed of one, three, and six benzimidazole and benzimidazolium units, respectively. The parent mono- or oligoimidazole is given a number  $X$  as identifier as shown in Figure 1. The neutral *N*-methylated imidazole analogue is named  $\text{Me}_n\text{X}$ , where  $n$  equals the number of methylated nitrogens in the compound. In analogy, the corresponding mono- or oligocationic imidazolium species is termed  $\text{Me}_{2n}\text{X}^{n+}$ , see Figure 1. The mono- or oligocation may interact with one or more monoanions  $\text{A}^-$  forming ionic assemblies/compounds identified as  $[\text{Me}_n\text{X}][\text{A}]_k^{(n-k)+}$ , where  $k$  is the number of anions bonded to the cation.

The organic triflate ( $\text{TfO}^-$ ) salt  $[\text{Me}_21][\text{TfO}]$  of 1,2,3-trimethylbenzimidazolium with the smallest cation  $\text{Me}_21^{1+}$  in the cation series was synthesized from commercially available 2-methylbenzimidazole 1 according to literature procedure.<sup>20</sup>

The second organic salt  $[\text{Me}_22][\text{TfO}]$  with the monocationic cation  $\text{Me}_22^{1+}$  was prepared by a similar route in two

subsequent *N*-alkylation steps from 2-phenylbenzimidazole 2. First, monoalkylation of 2 was accomplished by treatment with sodium hydride followed by quenching with methyl iodide (Scheme 1). The resulting 1-methyl-2-phenylbenzimidazole **Me2** was then subjected to methyl triflate to give the target salt  $[\text{Me}_22][\text{TfO}]$ . The organic salt  $[\text{Me}_63][\text{TfO}]_3$  with the tricationic cation  $\text{Me}_63^{3+}$  was prepared as reported previously from 1,3,5-tris(*N*-methylbenzimidazol-2-yl)benzene.<sup>16</sup>

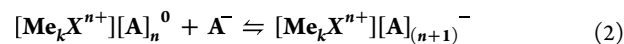
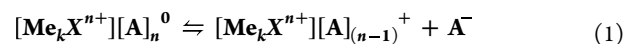
The synthesis of the organic salt  $[\text{Me}_{12}4][\text{TfO}]_6$  with the hexacation  $\text{Me}_{12}4^{6+}$  commenced with a Phillips–Ladenburg reaction between hexakis(4-carboxyphenyl)benzene<sup>21</sup> and *o*-phenylenediamine forming the requested hexakis[4-(benzimidazol-2-yl)phenyl]benzene 4 (Scheme 2). The condensation product was then methylated by a similar protocol as employed in the preparation of  $[\text{Me}_22][\text{TfO}]$ . Alkylation with methyl iodide gave an hexamethylated intermediate and subsequent treatment of this intermediate with methyl triflate produced the sought-after hexacationic  $[\text{Me}_{12}4][\text{TfO}]_6$ .

All four organic salts ( $[\text{Me}_21][\text{TfO}]$ ,  $[\text{Me}_22][\text{TfO}]$ ,  $[\text{Me}_63][\text{TfO}]_3$ , and  $[\text{Me}_{12}4][\text{TfO}]_6$ ) and their corresponding unmethylated neutral counterparts 1, 2, 3, and 4 were used in non-covalent functionalization of graphene according to our protocol published recently.<sup>16</sup> In our studies both graphene prepared by the CVD method<sup>13,22</sup> and r-oxo-G were used to enable reliable and complementary analyses.

**Cyclic Voltammetry.** The non-covalent functionalization of graphene with the organic salt  $[\text{Me}_63][\text{TfO}]_3$  caused a p-doping effect of the underlying graphene via a partial electron transfer from the graphene layer to the trication  $\text{Me}_63^{3+}$ .<sup>16</sup> To further our understanding about the reported doping process and the potential use of organic polycations as dopants, the redox properties of the four organic salts, together with their neutral precursors, were investigated by cyclic voltammetry. Cyclic voltammograms of all substances were measured at different sweep rates in DMF solutions. As an example, the voltammograms for the charged compounds at a sweep rate of  $1 \text{ Vs}^{-1}$  are shown in Figure 2.

In Table 1, reduction peak potentials are listed together with the reversible potentials determined by simulation, all referring to the  $\text{Ag}/\text{Ag}^+$  reference electrode used in the experiments. Experimental details and information about the simulations are described in the Supporting Information, see pages 24–33 and Figures S27–S37.

Electrolytic association–dissociation equilibria are expected to be established in the sample solutions before data acquisition start.



This guarantees complete exchange of anions,  $\text{A}^-$ , with the electrolyte, which assures that the same analytes are studied irrespectively of from which salt the samples have been prepared, see data for  $[\text{Me}_22][\text{BF}_4]$  in Table 1.

All organic cations have less negative reduction potentials than their neutral counterpart. However, none of the compounds have a reduction potential that is more positive than the oxidation potential for graphene; i.e., spontaneous oxidation of graphene will not take place. In the series of cationic  $\pi$ -conjugated molecules, the salt of monocationic  $\text{Me}_22^{1+}$  has the least negative reduction potential and should



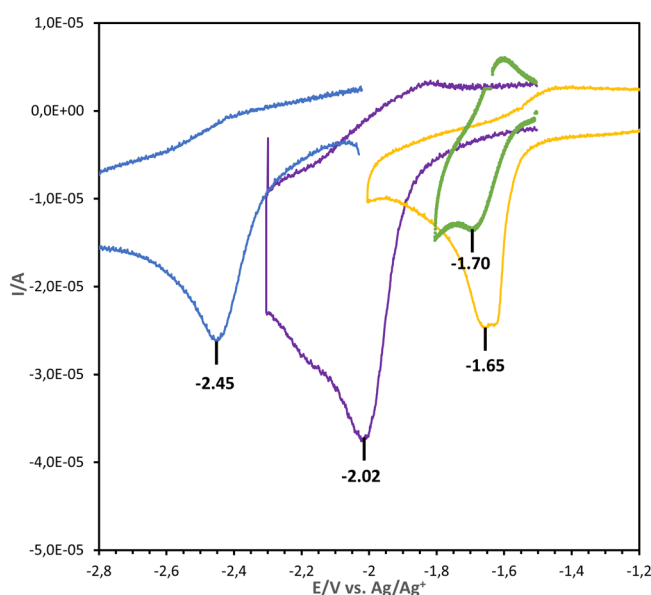


**Figure 2.** Cyclic voltammograms showing the first reduction peak of the organic salts  $[\text{Me}_21][\text{TfO}]$  (blue trace),  $[\text{Me}_{124}][\text{TfO}]_6$  (purple trace),  $[\text{Me}_63][\text{TfO}]_3$  (green trace), and  $[\text{Me}_22][\text{BF}_4]$  (yellow trace) in DMF. Concentration of active material 1 mM for  $[\text{Me}_21][\text{TfO}]$ ,  $[\text{Me}_22][\text{TfO}]$ , and  $[\text{Me}_63][\text{TfO}]_3$  and 0.5 mM for  $[\text{Me}_{124}][\text{TfO}]_6$ . Sweep rate  $1 \text{ V s}^{-1}$ . The peak potentials are marked in the figure and can also be found in Table 1.

**Table 1. Experimental and Simulated Reduction Potentials (in V)**

compound	$E_p^a$ vs $\text{Ag}/\text{Ag}^+$ (V)	$E_0^b$ vs $\text{Ag}/\text{Ag}^+$ (V)	figure <sup>c</sup>
1	-2.95	-2.6 to -2.8	S33
2	-2.70	-2.68	S34
3	-2.45	-2.39	S35
4	-2.64	-2.3 to -2.4	S36
$[\text{Me}_21][\text{TfO}]$	-2.45	-2.28	S32
$[\text{Me}_22][\text{BF}_4]^d$	-1.65	-1.58	S31
$[\text{Me}_63][\text{TfO}]_3$	-1.70	-1.65	S29
$[\text{Me}_{124}][\text{TfO}]_6$	-2.02	-1.90	S30

<sup>a</sup>Peak potentials in DMF at a scan rate of  $1 \text{ V/s}$ . <sup>b</sup>Obtained by simulations. <sup>c</sup>See figures in the Supporting Information (Figures S29–S36). <sup>d</sup>Cyclic voltammetry data were recorded for salts of  $\text{Me}_22^+$  with several different counterions. The differences in experimental results were within experimental errors.

be the compound most prone to accept electrons from the underlying graphene, Figure 2.

Within the series of salts,  $[\text{Me}_21][\text{TfO}]$  has the most negative reduction potential (Table 1, Figures 2 and S32). This salt contains the only cation in the series that lacks a phenyl group in the 2 position of the benzimidazolium moiety. The result highlights the stabilizing effect the phenyl ring exerts on the benzimidazolium species through electron delocalization.

The salt of the trication  $\text{Me}_63^{3+}$  shows the first reduction potential at  $E_{\text{red},1} = -1.65 \text{ V}$ . This cation shows some reversibility of the electron-transfer reaction (Figures 2 and S29). The reversibility diminishes with the decreasing sweep rate due to chemical follow-up reactions (see Figure S38).

The monocationic molecule  $\text{Me}_22^{1+}$  seems to be afflicted with some adsorption on the electrode, but it had a negligible influence on the recorded cyclic voltammetry data (Figures 2 and S31). Simulations and fitting of cyclic voltammetry curves

yield a reasonable diffusion coefficient of  $7 \times 10^{-6} \text{ cm}^2/\text{s}$  for this molecule (Figure S31). Simulation of the cyclic voltammetry curve for the tricationic molecule  $\text{Me}_63^{3+}$  shows three separate reduction peaks (Figure S37). The first electron transfer is quasi-reversible, which has been observed at different sweep rates (Figure S29). A chemical step follows the first reduction peak (EC mechanism) associated with a small rate constant. The subsequent second and third electron transfer reactions take place at different potentials, about 150 mV apart.

From the simulations, a diffusion coefficient of  $2.5 \times 10^{-6} \text{ cm}^2/\text{s}$  was obtained. For the tricationic molecule, the electron transfer reactions influence each other. This is in line with the DFT calculations, which show that lowest unoccupied molecular orbital (LUMO), i.e., approximately the electron density of the extra electron, is strongly localized on the central benzene ring and that the imidazolium units are electronically coupled (Figure 3). After adding one electron, the next

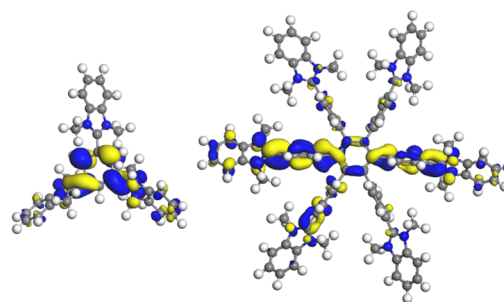


**Figure 3.** LUMO of  $\text{Me}_63^{3+}$  (PBE,<sup>19</sup> GGA functional/CASTEP basis set within the Material Studios framework) and hexacationic  $\text{Me}_{124}^{6+}$  (blue: positive phase of MO; yellow: negative phase of MO).

electron will be more difficult to add and the same for the third electron. Thus, we see three different reduction peaks. At even more negative potentials than the reduction potential of neutral molecule 3, additional reduction peaks are observed showing slight reversibility (Figure S37).

With the assumption that the electrochemical events for the cation–anion assembly of the hexacation  $\text{Me}_{124}^{6+}$  could be described using the same diffusion coefficient as obtained for  $\text{Me}_63^{3+}$ , the experimental data could be fitted to six consecutive two-step processes consisting of an electron transfer step followed by a chemical step. An equally good fit is obtained when fitted to six consecutive electron transfer reactions followed by one chemical step. The assumption of similar diffusion coefficients is based on the fact that the equivalent spherical diameter estimated for the two systems does not differ much. The redox potentials must be the same for all six electron transfer reactions or at less negative reduction potential for the second and subsequent steps. The more negative reduction potential of  $\text{Me}_{124}^{6+}$  compared to  $\text{Me}_22^{1+}$  and  $\text{Me}_63^{3+}$  can be explained by two cooperative effects. The dihedral angle between the core benzene ring and the attached appendages consisting of 1,3-dimethyl-2-phenylbenzimidazolium units efficiently isolates them electronically from each other. Furthermore, the appendages pairwise form pincerlike structures that efficiently can bind one anion each, see below. Tight ion pair formation may impair the electron-accepting ability of the system.

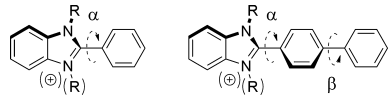
For the hexavalent molecule, the benzene ring in the center is largely unaffected and the six arms act independently (or

actually they are triply degenerated and screened from each other). This means that the electron transfers appear separately and from the formation energies it seems like the first electron transfer is the most difficult and the others, therefore, appear at the same potential (Figures 3 and S40).

Our DFT calculations support a reaction scheme in which each reduction step of the fully ion-paired or “dressed” hexacation  $\text{Me}_{12}\text{4}^{6+}$  is followed by the loss of one triflate ion before the next reduction event. Consequently, the corresponding CV displays only small shifts toward gradually less negative reduction potentials with each reduction event. This is in contrast with the CV for the trication that exhibits well-separated reduction potentials for the 1st, 2nd, and 3rd reduction steps indicating that the trication  $\text{Me}_6\text{3}^{3+}$  is not electrostatically shielded by anions to the same extent as is the “dressed” hexacation.

**DFT Calculations.** Geometry optimizations were performed using the PBE GGA density functional.<sup>19</sup> The polybenzimidazole/ium systems are all twisted, characterized by the dihedral angle between the benzimidazole/ium plane and the appended phenyl ring in the 2 position. This dihedral angle varies significantly within the series of molecules. The uncharged molecules are close to planar, and the organic cations are highly twisted, see Table 2.

**Table 2. Average Dihedral Angle between the Benzimidazole or Benzimidazolium Ring and the Next Neighboring Phenyl Ring in Optimized Structures of the Parent Systems ( $n+$ ) and the Systems with One Addition Electron ( $n - 1+$ )**



molecules	dihedral angle $\alpha$ (in $^\circ$ )	
	$\alpha(\text{M}^{n+})$	$\alpha(\text{M}^{(n-1)+})$
2	7	<1
3	5	2
4	8	8
$\text{Me}_2\text{2}^{1+}$	56	30
$\text{Me}_6\text{3}^{3+}$	58	50
$\text{Me}_{12}\text{4}^{6+}$	51 ( $\beta = 75^\circ$ )	45 ( $\beta = 64^\circ$ )

Energy-minimized structures of systems before and after addition of one additional electron, i.e., after reduction, were compared to reach a qualitative understanding of the dependence of the observed reduction potentials on the dihedral angle between the benzimidazole/ium moiety and the appended phenyl ring. The average dihedral angles in the optimized structures are given in Table 2.

The comparisons show that all the reduced species have smaller dihedral angles than the parent oxidized form. This is indicative of a stabilizing effect on the open shell system, formed upon addition of an electron, exerted by the phenyl ring in the 2 position through conjugation. The smaller the dihedral angle is, the larger the electronic coupling between the two moieties becomes, resulting in a stronger stabilizing effect. It is also consistent with the bonding nature of the LUMO orbital, which becomes partly filled upon reduction, between the carbons linking the benzimidazolium moiety and the phenyl ring together.

The largest geometrical changes are observed for the cationic systems. The change in dihedral angle before and after addition of an electron is the largest for  $\text{Me}_2\text{2}^{1+}$ . The optimized dihedral angle of  $\text{Me}_2\text{2}^{1+}$  is  $56^\circ$ . The optimal dihedral angle decreases to  $30^\circ$  for the uncharged radical system  $\text{Me}_2\text{2}^\bullet$ , formed upon addition of one electron. This is the smallest dihedral angle adopted by any of the cationic systems reduced by one electron. The small dihedral angle in the optimal conformation of the reduced product, in combination with the positive charge of the parent compound and the ability of the system to undergo large conformational adjustments, indicates that this system should readily accommodate one additional electron. This is corroborated by the least negative reduction potential observed for the studied systems.

The largest twist angle of all systems was found for the tricationic  $\text{Me}_6\text{3}^{3+}$ , which has a propeller-shaped geometry characterized by an average dihedral angle of  $58^\circ$ . The conformational change upon addition of one additional electron to form the reduced radical dication  $\text{Me}_6\text{3}^{2+}$  is small. The optimal dihedral angle for the reduced species is  $50^\circ$ , which is the largest dihedral angle found for any of the reduced forms of the investigated systems. According to the shape of the calculated LUMO (Figure 3), much of the radical spin density is localized on the central aryl ring bridging the three benzimidazolium moieties. These results suggest that the trication may be less prone to accept an electron compared to the monocation. This is corroborated by the somewhat more negative reduction potential measured for the trication compared to that of the monocation.

The smallest difference in the dihedral angle between the benzimidazolium plane and the plane of the neighboring phenyl ring before and after reduction among the cationic systems is found for the hexacation  $\text{Me}_{12}\text{4}^{6+}$ . The dihedral angle in the hexacationic system is  $51^\circ$  and decreases to  $45^\circ$  for the radical pentacationic system  $\text{Me}_{12}\text{4}^{5+}$ . The relatively large dihedral angle in the reduced species may in part explain the more negative reduction potential compared with those observed for the other phenyl-substituted benzimidazolium systems. However, a direct comparison is not possible. The change in the dihedral angle between the benzimidazolium plane and the neighboring phenylene ring is accompanied by a change in the dihedral angle between the planes of the core benzene ring and the surrounding bridging phenylene rings. The synergetic effect of these changes is difficult to interpret. Both decreases upon addition of an extra electron, which should favor electronic stabilization. The dihedral angle between the core benzene ring and the surrounding phenylene groups decreases from  $75$  to  $64^\circ$ . Interestingly, combining these decreases in dihedral angles increases the dihedral angle between the benzimidazolium plane and the plane of the core benzene ring from  $54$  to  $71^\circ$ . Thus, in contrast to the trication that planarizes upon addition of an extra electron, the hexaimidazolium propeller-shaped structure becomes more twisted upon addition of one electron.

Structurally, the neutral molecules 2, 3, and 4 show the same behavior as the cations although they are almost flat already before addition of the extra electron. Again, the smallest system 2 shows the strongest relative planarization of all tested neutral molecules. However, the geometrical adjustment of the already almost planar molecule does not compensate for the smaller  $\pi$ -conjugated system in the stabilization of an extra electron, as can be seen by the less negative reduction potentials for the

compounds with larger  $\pi$ -conjugated systems. The dihedral angles between the imidazole units and the next neighboring phenylene rings in hexabenzimidazole compound **4** do not change. Instead, the dihedral angles between the core benzene ring and its surrounding phenylene rings are decreased, allowing for better stabilization through conjugation.

The computational study presented above dealt only with naked cations disregarding the effect of the counterion. The molecular structure of the hexacation  $\text{Me}_{12}\text{4}^{6+}$  contains six pincer-like clefts, three on either side of the oblate-spheroidal structure, in which the triflate ions can bind. Upon binding, the anions form tight ion pairs with the benzimidazolium units that constitute the walls of the clefts, see Figure 4. We believe that this structural feature plays a decisive role in shaping the electrochemical properties of this salt and its behavior as an adsorbate.

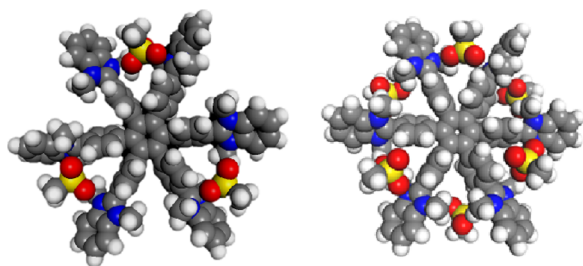
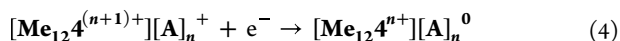


**Figure 4.** Optimized structure of the hexacation  $\text{Me}_{12}\text{4}^{6+}$  together with three (left) and six (right) triflate counterions.

The chemical follow-up reactions of imidazoline radicals, formed by one-electron reduction of imidazolium compounds, have been attributed to radical decomposition into the corresponding carbenes and to dimerization of the radical intermediates (Figures S38 and S39, Table S5).<sup>23,24</sup> A phenyl substituent in the 2 position stabilizes, to a greater extent than a methyl group, the imidazole radical and suppresses both radical decomposition and dimerization, see the Supporting Information. Indeed, dimers of 2 substituted benzimidazoline radicals have been used as effective n-dopants for organic semiconductors.<sup>17,18</sup> The dimeric dopants undergo dissociation at room temperature to the parent radicals, which during the doping process form the corresponding stable benzimidazolium cations. For the hexabenzimidazolium system, the dimerization is not only thermodynamically less favorable but also kinetically disfavored by steric encumbrance. Here, we have explored alternative follow-up reaction pathways for the hexabenzimidazolium system.

The energetics of the six reduction steps for the hexabenzimidazolium system were addressed to make contact with our cyclic voltammetry experiments. Specifically, the impact of counterions on the reversible redox process was sought.

Three different mechanisms for the reduction of the cation–anion assembly were evaluated. The first mechanism consists of a preceding homogenous chemical reaction (electrolytical dissociation) coupled to an electron transfer step,  $\text{C}_r\text{E}_r$ :



This was deemed to be inconsistent with experimental data. The trend observed for the recorded cyclic voltammograms is

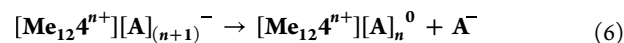
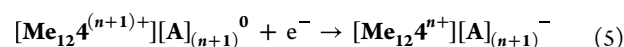
not consistent with the expected less negative peak potential and decreasing current function with an increasing scan rate expected for a CE mechanism. The other two mechanisms were evaluated by comparing experimental cyclic voltammetry data with energetics obtained by DFT calculations, see Table 3.

**Table 3.** Total Energies,  $E_{\text{Calc}}$ , Calculated for Salts  $[\text{Me}_{12}\text{4}^q][\text{A}]_n^{(q-n)}$  with different Oxidation Numbers,  $q$ , of the Cation and Varying Number of Anions,  $n$ , Together with Electron Affinities, EA, Derived from the Total Energies

chemical compound [Me <sub>12</sub> 4 <sup>q+</sup> ] [A] <sub>n<sup>(q-n)</sup></sub>	$E_{\text{Calc}}(n,q)$ (Ha)		EA <sup>a</sup> (eV)
	$q = n$	$q = n - 1$	
n			
6	−8342.538833	−8342.616840	2.12
5	−7679.040128	−7679.115443	2.05
4	−7015.538560	−7015.616306	2.12
3	−6352.047615	−6352.112588	1.77
2	−5688.543648	−5688.599516	1.52
1	−5025.036171	−5025.089703	1.46
0	−4361.461166		

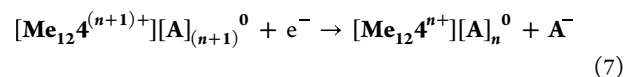
<sup>a</sup>Calculated as  $E_{\text{Calc}}(n,q = n + 1) - E_{\text{Calc}}(n,q = n)$  using 1 Ha = 27.21138 eV.

The second mechanism assessed is composed of a reversible electron transfer step followed by an irreversible homogenous chemical reaction (strongly favored electrolytical dissociation),  $\text{E}_r\text{C}_i$ :



Assuming that the electrolytical dissociation is strongly favored and that the species so formed is equally or even more easily reduced than previous redox active species then, in agreement with the experimental results, a six-electron wave should be observed for the overall reduction sequence. The DFT calculations disclosed that the six reduction steps necessary to reduce the organic cation from six plus to a neutral species, in a vacuum, via this mechanism are rather isoenergetic (see the Supporting Information for more details and Figures S41 and S42). The differences between the reduction potentials of two consecutive  $\text{E}_r\text{C}_i$  reactions were approximated as the difference in reaction energies,  $\Delta E$ , between two consecutive reduction reactions, see Table 4.

The third mechanism considered is an irreversible concerted process in which the anion and the electron transfer occurred in the same step,<sup>25</sup> concerted chemical anion loss and electron transfer:



This mechanism represents the limiting case of the  $\text{E}_r\text{C}_i$  mechanism for the situation in which the rate of the second step is infinitely high. Approximate differences between the reduction potentials of two consecutive CAET reactions were calculated similarly as for the second mechanism. The pairwise differences in driving force for the five first reduction steps vary between −0.3 and 0.4 eV. A much larger difference of 1.8 eV was calculated for the difference between the last reduction



Table 4. Difference in Reaction Energies,  $\Delta E$ , between Two Consecutive Reactions

j	reaction energy differences	energy difference	
	$[\text{Me}_{12}\text{A}^{(j+1)+}][\text{A}]_{(j+1)}^0 \rightarrow (\rightarrow) [\text{Me}_{12}\text{A}^{(j-1)+}][\text{A}]_{(j-1)}^0$	$\Delta E_{\text{EC}}^a$ (eV)	$\Delta E_{\text{CAET}}^b$ (eV)
5	$E(n = 5 \rightarrow 4) - E(n = 6 \rightarrow 5)$	0.07	0.08
4	$E(n = 4 \rightarrow 3) - E(n = 5 \rightarrow 4)$	-0.07	-0.28
3	$E(n = 3 \rightarrow 2) - E(n = 4 \rightarrow 3)$	0.35	0.35
2	$E(n = 2 \rightarrow 1) - E(n = 3 \rightarrow 2)$	0.25	0.10
1	$E(n = 1 \rightarrow 0) - E(n = 2 \rightarrow 1)$	0.06	1.84

<sup>a</sup>Calculated as  $\Delta E_{\text{EC}} = E_{\text{Calc}}(n = j, q = n - 1) + E_{\text{Calc}}(n = j + 1, q = n) - E_{\text{Calc}}(n = j, q = n) - E_{\text{Calc}}(n = j + 1, q = n - 1) = EA_{(j+1)} - EA_j$ . <sup>b</sup>Calculated as  $\Delta E_{\text{CAET}} = E_{\text{Calc}}(n = j + 1, q = n) + E_{\text{Calc}}(n = j - 1, q = n) - 2E_{\text{Calc}}(n = j, q = n)$  using 1 Ha = 27.21138 eV.

step, reducing the cation from plus one to a neutral species, and the next-to-last reduction step, from two to one plus. Thus, the pairwise comparisons indicate that a second peak, corresponding to the sixth reduction step, should be observed at more negative potential alongside a possible five-electron peak. This is not observed. It appears that the second mechanism is the more plausible of the three explored.

Having understood the properties of the individual molecular system, we next explored the interaction between this system and graphene. The density of states and sum-over-states calculations were performed to probe the presence of charge transfer in the hybrid systems composed of graphene and the hexacation together with a various number of anions. These calculations show that the acceptor levels in the hexacation stay above the Fermi level of all hybrid systems, even for the most extreme hybrid system comprising unshielded hexacation without any anions (see Figures S42 and S43). The Fermi level for all hybrid systems corresponds to the top of the valence band of the graphene component. Thus, the signature of charge transfer present in the hybrid system of the previously studied trication<sup>16</sup> is clearly absent in the hybrid systems of the hexacation.

In fact, the highest energy states of the cation–ion cluster correspond to the HOMOs of the anions. The pivotal role of the anions is twofold. Not only do they allow for the formation of a neutral entity that interacts more favorable with the non-polar graphene surface than more polar media that dissolve the salt, but they also contribute sizeable polarizability to the resulting physisorption of the hexacation–anion complex to graphene.

The important role the triflate ions play in determining the properties of the hexacationic system is further underscored by our XPS studies of this system as an adsorbate on graphene.

**Raman Spectroscopy.** This technique was applied to establish that the organic salts adhere to the CVD graphene surface and to make a qualitative estimate of their doping ability. CVD graphene was used because the substrate, i.e., SiO<sub>2</sub>/Si wafer, is completely covered by graphene, and the Raman peaks are sharper compared to the peaks for r-oxo-G. This simplifies the Raman measurements, circumvents signals from the substrate, and reduces interfering overlap with other peaks in the subsequent analysis.

Samples of the organic salts [Me<sub>2</sub>1][TfO], [Me<sub>2</sub>2][TfO], and [Me<sub>3</sub>3][TfO]<sub>3</sub>, drop-cast on SiO<sub>2</sub>/Si wafers gave Raman spectra with sharp peaks. The spectrum of the sample with the organic salt [Me<sub>2</sub>1][TfO] on CVD graphene, prepared by the described wet-chemical procedure, did not display any significant peaks other than the two prominent G and 2D bands characteristic of CVD graphene at about 1584 and 2682 cm<sup>-1</sup>, respectively.<sup>26</sup> Possibly because the organic salt [Me<sub>2</sub>1][TfO] does not bind at sufficiently high concentrations

at the graphene surface to be detectable. The peaks from the salts in the spectra recorded for both [Me<sub>2</sub>2][TfO] and [Me<sub>3</sub>3][TfO]<sub>3</sub> on CVD graphene were clearly visible but substantially broadened compared to the spectra recorded for the corresponding SiO<sub>2</sub>/Si samples (Figure S25). Inhomogeneous broadening is observed for amorphous samples, where the chemical composition, crystal size, morphology, or local environmental vary significantly for different areas on the sample. Broadening can also be caused by the interaction between adsorbate and graphene.

Analysis of the peak area, intensity, position, and full width at half-maximum (FWHM) of the G and 2D peaks of graphene in Raman spectra can be used to provide information of the doping effect exerted by dopants. Since the broad molecular peaks in Raman spectra of the organic salts [Me<sub>2</sub>2][TfO] and [Me<sub>3</sub>3][TfO]<sub>3</sub> overlap with the doping sensitive G peak of graphene, a detailed statistical peak analysis is only possible for the 2D peak (Figure S24). The analysis shows that neither the organic salt [Me<sub>2</sub>1][TfO] nor [Me<sub>2</sub>2][TfO] significantly changes the position of the 2D peak. They do cause a slight decrease of the FWHM of the 2D peak. For the salt of the trication, [Me<sub>3</sub>3][TfO]<sub>3</sub>, both a large shift in position and some broadening of the 2D peak were observed.<sup>16</sup> Thus, the Raman spectroscopy study indicates that there is only a weak electronic interaction between graphene and the salt of the monocation, whereas the salt of the trication interacts more strongly.

Interfering fluorescence from the organic salt [Me<sub>12</sub>4]-[TfO]<sub>6</sub>, on both the naked SiO<sub>2</sub>/Si substrate and CVD graphene, made it impossible to perform Raman measurements with the available instrumental setups.

**ToF-SIMS.** Imaging ToF-SIMS was applied as a complement to Raman spectroscopy to establish the presence of non-covalently bound molecules on the surface of graphene.<sup>16</sup> Studying r-oxo-G flakes as substrate we recently showed that the anions, cations, and ionic derivatives of the cation were specifically detected on the surface of r-oxo-G flakes, while absent on the surrounding SiO<sub>2</sub>/Si substrate.

Similarly to what we reported on for [Me<sub>3</sub>3][TfO]<sub>3</sub>, ToF-SIMS imaging of samples with the organic salt [Me<sub>2</sub>2][TfO] on r-oxo-G shows signals corresponding to both the cation and the anion, but only at the areas ascribed to the r-oxo-G flakes (Figure S26).

In our study, an area of 150 μm × 150 μm of a film of functionalized flakes of r-oxo-G on SiO<sub>2</sub>/Si substrate was scanned in both positive and negative ion modes. The triflate ion TfO<sup>-</sup> with *m/z* = 148.95, the counterion to the cations, was detected in negative ion mode with a high signal/noise ratio as is shown in Figure 5A for r-oxo-G non-covalently functionalized with the organic salt [Me<sub>12</sub>4][TfO]<sub>6</sub>. The signal from the triflate ion is exclusively observed at the r-oxo-G

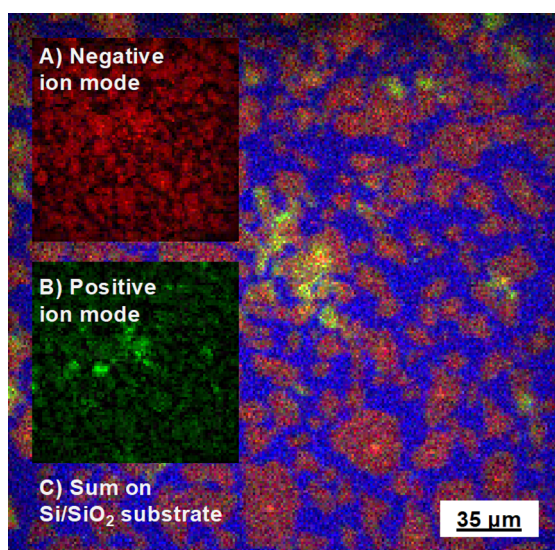


**Figure 5.** ToF-SIMS image in (A) negative ion mode showing the triflate anion  $\text{TfO}^-$  from the organic salt  $[\text{Me}_{12}\text{4}][\text{TfO}]_6$  on r-oxo-G in a flake-like pattern (red:  $m/z$  148.95) on  $\text{SiO}_2/\text{Si}$  substrate (blue color). (B) Positive ion mode fragments (green:  $m/z$  see text) from the hexacation  $\text{Me}_{12}\text{4}^{6+}$  were detected on the same areas as the triflate anion as seen in (C) color overlay image of ions recorded in negative (red) and positive (green) modes, respectively.

flakes and not on the  $\text{SiO}_2/\text{Si}$  substrate surface between the flakes (Figure 5, blue).

However, mass spectrometric identification of the hexacation  $\text{Me}_{12}\text{4}^{6+}$  is not trivial. The most intense peak in the mass spectrum recorded for the triflate salt of the hexacation  $\text{Me}_{12}\text{4}^{6+}$  by the gentle ionization method in electrospray ionization-mass spectrometry is found at  $m/z = 234,2799$ . This signal corresponds to the  $\text{M}^{6+}$  species and shows the expected isotope pattern (Figure S22). ToF-SIMS causes a high degree of fragmentation and adduct formation. The highest signal

intensities recorded in positive ion mode for  $[\text{Me}_{12}\text{4}][\text{TfO}]_6$  on r-oxo-G samples are found at  $m/z = 126.93, 360.80, 362.80,$  and  $596.66$ . In the same way as for the signals from the anion, these signals were only detected on the flake-like areas observed in the imaging mass spectrometry measurements (Figure 5B, green color).

Imaging ToF-SIMS clearly shows that the triflate salts of the monocation and the trication selectively/preferentially adhere to the r-oxo-G flakes in the wet-chemical dyeing process. Further, it provides strong indications that the dyeing process also brings about an adhesion of the salt of the hexacation. This is corroborated by the XPS data discussed below.

**XPS.** XPS was used to study the effect of the interaction between graphene and neutral molecules or organic salts, as well as to determine the elemental composition of the surface of the CVD-graphene/hybrid materials.<sup>27</sup> Spectra were recorded of the synthesized  $\pi$ -conjugated systems deposited on two different substrates, i.e., CVD graphene and  $\text{SiO}_2/\text{Si}$  (Figure 6).

In agreement with the chemical structure of graphene, the XPS spectrum of pristine graphene on  $\text{SiO}_2/\text{Si}$  substrate only shows one major C 1s peak centered at 284.6 eV,<sup>28</sup> together with a minor contribution from carbons in certain oxidation states that cannot be completely avoided during the preparation, mainly carbon signals from polymethylmetacrylate residues.<sup>28,29</sup> For more information see the Supporting Information. The binding energy of the main peak is consistent with the  $\text{sp}^2$ -hybridized character of the carbon present in graphene. Other observed signals correspond to silicon (Si) and oxygen (O), at 104 and 533 eV, respectively,<sup>30</sup> originating from the  $\text{SiO}_2$ -intersurface in between the graphene layer and silicon substrate. The weak nitrogen (N) signal observed at 400 eV<sup>30</sup> corresponds to the adsorbed molecular nitrogen. The intensity of the latter is small and has negligible effects on the subsequent molecular analysis. An overview of the complete N 1s analysis of all molecules is collected in Table S4.

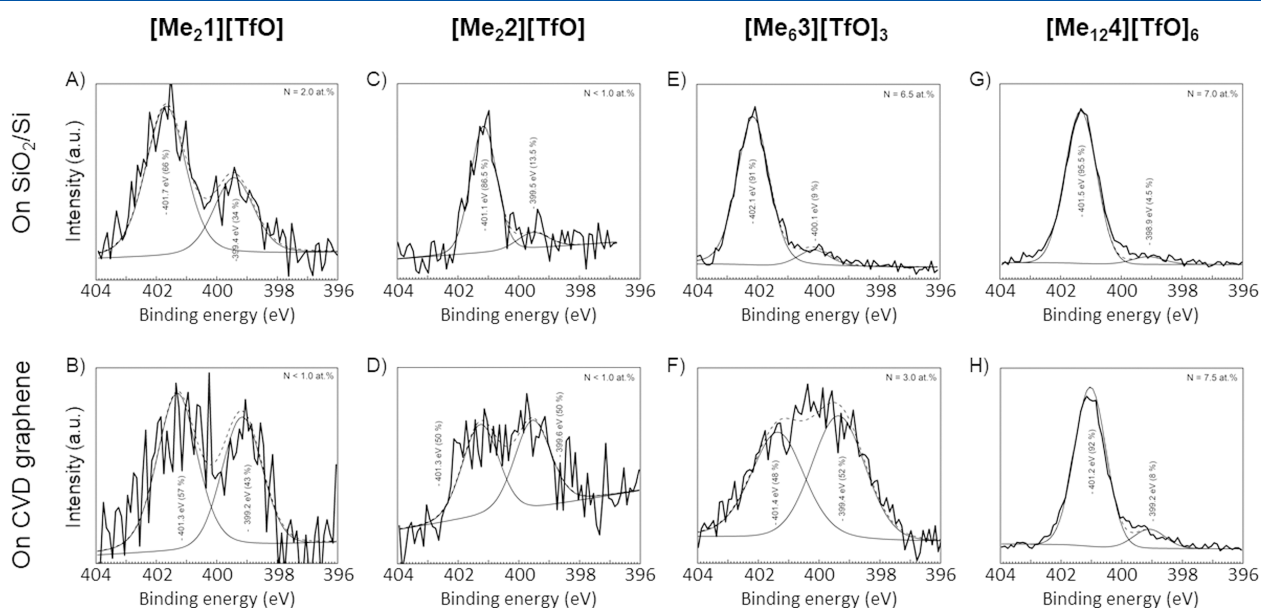


**Figure 6.** High resolution scan of the N 1s region of  $[\text{Me}_2\text{1}][\text{TfO}]$  on (A)  $\text{SiO}_2/\text{Si}$  surface and (B) on CVD graphene;  $[\text{Me}_2\text{2}][\text{TfO}]$  on (C)  $\text{SiO}_2/\text{Si}$  surface and (D) on CVD graphene;  $[\text{Me}_6\text{3}][\text{TfO}]_3$  on (E)  $\text{SiO}_2/\text{Si}$  surface and (F) on CVD graphene;  $[\text{Me}_{12}\text{4}][\text{TfO}]_6$  on (G)  $\text{SiO}_2/\text{Si}$  surface and (H) on CVD graphene.



All neutral imidazole systems contain two sets of chemically different nitrogen atoms, i.e., imine type of nitrogen atoms ( $R_2C=N-R$ ) and secondary amine type of nitrogen atoms ( $R_2-NH$ ). Thus, these systems are expected to display two distinct peaks in the N 1s spectra.<sup>31,32</sup> On the other hand, all nitrogen atoms in the cationic systems are chemically equivalent, i.e., a single N 1s peak corresponding to an imidazolium nitrogen is expected to be found in the XPS spectra recorded for organic salts.<sup>33–35</sup> An overview of all N 1s spectra recorded for samples on both SiO<sub>2</sub>/Si and CVD graphene substrates incubated with the organic salts [Me<sub>2</sub>1]-[TfO], [Me<sub>2</sub>2][TfO], [Me<sub>6</sub>3][TfO]<sub>3</sub>, and [Me<sub>12</sub>4][TfO]<sub>6</sub> is shown in Figure 6. An overview of the N 1s spectra of the neutral systems is attached in the Supporting Information (Table S1).

The N 1s spectra for both the neutral and the charged systems on SiO<sub>2</sub>/Si substrate are in line with what is expected for these systems. For example, the spectrum of **2** exhibits two deconvoluted peaks in a 1:1 area ratio and with the binding energies of 398.7 and 400.0 eV, respectively, while the spectrum of [Me<sub>2</sub>2][TfO] exhibited one major peak at 401.1 eV (Figure 6C). The energy difference between the two N 1s peaks observed for the neutral molecules varies among the studied compounds. Further, the binding energies of the two peaks vary with the substrate onto which the molecules are adsorbed. On SiO<sub>2</sub>/Si substrate, the energy difference is the lowest for monobenzimidazole compound **2** with 1.3 eV, and it is the largest for the tribenzimidazole compound **3** with 2.1 eV. The energy difference observed for the hexabenzimidazole compound **4** is 1.5 eV. The energy differences between the two peaks observed for **2** and **3** on CVD graphene are the same as found for the SiO<sub>2</sub>/Si samples. In contrast, the energy difference between the two N 1s peaks recorded for the hexabenzimidazole compound **4** on CVD graphene is 1.8 eV, 0.3 eV larger than that observed for the corresponding SiO<sub>2</sub>/Si sample. The measured core level N 1s binding energies are overall higher (0.1–0.4 eV) for the neutral benzimidazole-CVD graphene systems than for the neutral benzimidazole-SiO<sub>2</sub>/Si systems, as can be seen in Table S4, except for the peak of lowest binding energy observed for compound **4**. It is shifted toward lower binding energy on CVD graphene by 0.2 eV.

Interestingly, the nitrogen concentration for tribenzimidazole compound **3** is a factor of 3 higher compared with the other neutral molecules (**2**, **4**) on CVD graphene. This indicates that molecule **3** binds more strongly to graphene than the other neutral compounds. This observation is in line with the overall planar geometry of the molecule in combination with its large size, which leads to strong dispersive interactions between **3** and graphene. Obviously, the larger size of compound **4** does not fully compensate for its twisted molecular geometry disfavoring the binding interactions (Tables 2 and 5).

All samples with organic salts on SiO<sub>2</sub>/Si substrate exhibit, as expected, one major peak in the recorded N 1s spectra (Figure 6). In all spectra, the major peak is accompanied by a weak peak, at lower binding energy, of unknown origin. Possibly signals from minor ensembles of molecules in unordered or differently packed arrangements compared to the bulk of molecules.

Another possibility is that a small fraction of the counterion is lost upon binding and compensated by negatively charged silanolate groups on the SiO<sub>2</sub>/Si surface leaving some

**Table 5. Theoretical and Observed Atomic Ratios for the Elements F and N in Samples of Imidazole Compounds and Imidazolium Salts on SiO<sub>2</sub> and CVD Graphene, Together with Calculated Surface Coverages and Relative Binding Constants**

species	atomic ratio <sup>a</sup> (%)			surface coverage $\theta^b$
	theoretical		$\frac{x_F}{x_N}$	
	$x_F$	$x_N$		
<b>1</b>	0	20.0	0	(5.0)
SiO <sub>2</sub> /Si		16.5		82.5
CVD graphene		2.0		10.0
<b>2</b>	0	13.3	0	(7.5)
SiO <sub>2</sub> /Si		7.0		52.6
CVD graphene		3.0		22.6
<b>3</b>	0	18.2	0	(5.5)
SiO <sub>2</sub> /Si		13.5		74.3
CVD graphene		10.5		57.8
<b>4</b>	0	12.5	0	(8.0)
SiO <sub>2</sub> /Si		3.5		28.0
CVD graphene		3.0		24.0
[Me <sub>2</sub> 1][TfO]	15.0	10.0	1.5	(10.0)
SiO <sub>2</sub> /Si	9.0	2.5	3.6	25.0
CVD graphene	n.d.	< 1.0		<10.0
[Me <sub>2</sub> 2][TfO]	12.0	8.0	1.5	(12.5)
SiO <sub>2</sub> /Si	2.0	1.0	2.0	12.5
CVD graphene	n.d.	2.5	0	31.2
[Me <sub>6</sub> 3][TfO] <sub>3</sub>	14.3	9.5	1.5	(10.5)
SiO <sub>2</sub> /Si	9.0	7.0	1.3	73.5
CVD graphene	1.0	3.5	0.3	36.8
[Me <sub>12</sub> 4][TfO] <sub>6</sub>	11.5	7.7	1.5	(13.0)
SiO <sub>2</sub> /Si	10.0	8.5	1.2	110.5
CVD graphene	10.5	7.5	1.4	97.5

<sup>a</sup>Atomic ratio is calculated as  $x_j = \frac{n_j}{\sum n_j}$ , where  $j = C, F, N, O$ , and  $S$ . H omitted because it is untraceable in XPS. <sup>b</sup>Assumed uniform signal intensity across the sample area.  $\theta = \frac{I_a^X}{x_X} 100$ , where  $I_a^X$  is the peak area recorded for element  $X$  and  $x_X$  is the atomic ratio of element  $X$  in its molecular formula.

molecules unshielded. The energy differences between the major and minor N 1s peaks vary. The largest difference of 2.6 eV is observed for the hexabenzimidazolium salt [Me<sub>12</sub>4]-[TfO]<sub>6</sub> and the smallest of 1.6 eV for the monobenzimidazolium salt [Me<sub>2</sub>2][TfO].

In contrast, upon interaction with CVD graphene all organic salts, except the hexabenzimidazolium salt [Me<sub>12</sub>4][TfO]<sub>6</sub>, display two peaks of comparable size in the N 1s spectra or signals that can be deconstructed into two components of equal weight. The hexabenzimidazolium salt [Me<sub>12</sub>4][TfO]<sub>6</sub> displays a spectrum with one major peak, very similar to the spectrum recorded for the same adsorbate on SiO<sub>2</sub>/Si substrate.

The energy difference between the two peaks observed in the spectra of the mono- and the tribenzimidazolium salts are the same as observed for these salts on SiO<sub>2</sub>/Si substrate. The peak broadening and the requirement of at least two peaks to fit the experimental data may be explained by a combination of two reasons. First, the equal weight may suggest that the two different binding energies are observed because the nitrogen atoms are differentiated into two sets exposed to different chemical environments upon non-covalent binding to

graphene due to the twisted geometry of the monocationic molecule  $\text{Me}_2\text{2}^{1+}$  and the propeller-like geometry of the tricationic  $\text{Me}_6\text{3}^{3+}$ . One nitrogen atom in each imidazolium unit of the molecules is facing the graphene surface, and the other nitrogen atom is pointing away from the graphene surface. However, the highly twisted hexacationic  $\text{Me}_{12}\text{4}^{6+}$  gives rise to only one N 1s signal. Therefore, a more reasonable explanation is that different ensembles of adsorbates experience varying Coulombic fields generated by cations accompanied by a varying number of anions.

Notably, the spectrum of the hexabenzimidazolium salt  $[\text{Me}_{12}\text{4}][\text{TfO}]_6$  on CVD graphene indicates a substantially higher nitrogen content compared to the other CVD graphene samples. Thus, graphene shows a higher affinity for this system than any other of the systems studied. The elemental composition of surfaces can be analyzed with XPS.

We analyzed the XPS spectra with respect to the N 1s and F 1s signals to calculate the ratio between the number of anions and cations on the surfaces. This is possible because nitrogen is only present in the cations of the organic salts and fluorine is only present in the anions. The F 1s fluorine signal is observed at 688.4 eV for both the sample on  $\text{SiO}_2/\text{Si}$  substrate and on CVD graphene and corresponds to an organic fluoride. The ratio between the areas for the nitrogen and fluorine signals (N/F) agrees with the molecular formula for all organic salts on  $\text{SiO}_2/\text{Si}$  substrate (Table S2). However, XPS spectra recorded for CVD graphene samples indicate a lower fluorine content than expected, except for the salt of the hexacation. Therefore, we suggest that the smaller organic salts lose some counterions in the process of binding to graphene. This can be explained by an ion exchange during the sample incubation or by the already mentioned partial charge transfer between graphene and the organic cations. This partial electron transfer leads to weaker Coulomb attractions between the cation and its surrounded counterion(s). Formation of two-dimensional metal salt crystals on r-oxo-G with abnormal, anion-deficient stoichiometric compositions has been reported.<sup>36</sup> In analogy with the organic salts studied in this paper, the abnormal stoichiometries of these crystals were attributed to the cation- $\pi$  interaction between the metal cations and the  $\pi$ -system of r-oxo-G.

Sulfur is also only present in the anion, and an analogous analysis based on this element gives the same result. However, the sulfur content in most of the samples was under the detection limit, i.e., <1.0 atomic %. On the other hand, analysis of the spectrum of the organic salt  $[\text{Me}_{12}\text{4}][\text{TfO}]_6$  on CVD graphene indicates no or very little loss of triflate anions. This could be the result of tight ion pairing thanks to the pincer like structure of the hexacation. In effect, the disc-like entity binds to graphene as a large neutral species without sharing its electrons with the CVD graphene, i.e., without the partial electron transfer.

## CONCLUSIONS

We have prepared two related series of compounds: one series of neutral molecules composed of one, three, or six benzimidazole units and a second series of organic salts with cations comprising one, three, or six benzimidazolium groups. The three or six identical elements of the larger members in each series are assembled around a central core consisting of a benzene ring and a hexaphenylbenzene, respectively. Thus, the common structural elements within these series are 2-

phenylbenzimidazole and 2-phenylbenzimidazolium, respectively.

The reduction potentials within the neutral series show only a small variation. The corresponding cations are all reduced at less negative potentials. Despite the intermediate-sized system having two more positive charges than the smaller one, both have comparable reduction potentials. Surprisingly, the largest molecular ion  $\text{Me}_{12}\text{4}^{6+}$  with six positive charges is the hardest to reduce. The more negative reduction potential of the hexacation is attributed to the poor electronic coupling between the benzimidazolium units due to the large twist angle between the core benzene ring and its benzimidazolium-containing appendages. In addition, supported by quantum mechanical modeling, these benzimidazolium-based appendages pairwise form a tweezer-like structure that effectively accommodates the counterion causing tight ion pairing. Based on the reduction potentials for these compounds, neither of them should undergo a charge transfer process with graphene.

Graphene surfaces were functionalized non-covalently by immersion in methanol solutions of the respective compounds of the two series. Imaging mass spectrometry reveals that the compounds adhere only to the flakes of r-oxo-G during the dyeing process and not on the silicon dioxide support on which the flakes rest. XPS studies of non-covalently functionalized CVD graphene samples show that there is no general preference in affinity of graphene for adsorbates from either of the two series of neutral and cationic compounds (neutral compounds and organic salts). Of the neutral molecules, the highest affinity is found for the intermediate sized 3. We suggest that the flat structure of this compound enables short binding distance and favorable London dispersion interactions. The weaker interaction between graphene and the larger 4 molecule is due to the longer binding distance enforced by the twist angle between the core benzene ring and its appendages.

Analysis of the XPS data unveils that the organic salts, except for the largest hexacationic salt  $[\text{Me}_{12}\text{4}][\text{TfO}]_6$ , lose a large fraction of their original counteranions upon interaction with graphene. The degree of surface coverage appears to be limited by the balance between adsorbates' binding energy and the Coulomb repulsion between the charged adsorbates and/or between the electron affinity of the adsorbate and the increase in work function (p-doping) of graphene with increased surface coverage. Thus, the binding of the mono- and tricationic salts displays a negative cooperativity.

Of the tested compounds, the highest affinity of graphene is for the hexacationic salt  $[\text{Me}_{12}\text{4}][\text{TfO}]_6$ . This salt appears to bind to graphene as an uncharged disk-shaped entity in which there is a tight ion pairing between the hexacation and its six counterions. Thus, although seemingly highly charged, the interaction of  $[\text{Me}_{12}\text{4}][\text{TfO}]_6$  with graphene is governed by London dispersion interactions. We found no experimental evidence for charge transfer between graphene and the hexacation.

In summary, we have shown that the affinity of graphene for binding an adsorbate is in general not favored by positive charges on the adsorbate, nor is it only dependent on the size of the adsorbate. The three-dimensional structure of the adsorbate plays a decisive role. Further, if the adsorbate is ionic, then both the anion and the cation and the interaction between them influence the binding. We have also shown that salts of organic cations can lose their counterion(s) on binding to graphene and that this loss of anions can be prevented by proper design of the organic cation.

We expect this finding to be important in the future design of materials used in the preparation of new functionalized 2D materials with defined electronic properties.

## ■ ASSOCIATED CONTENT

### SI Supporting Information

The Supporting Information is available free of charge at <https://pubs.acs.org/doi/10.1021/acs.jpcc.2c07643>.

Experimental details and spectroscopic data for all new compounds: NMR spectra, HR-MS spectra, cyclic voltammograms; preparation details and characterization of functionalized single-layer graphene samples: Raman spectra, X-ray photoelectron spectra, ToF-SIMS images; and computational details (PDF)

## ■ AUTHOR INFORMATION

### Corresponding Author

**Jerker Mårtensson** – Department of Chemistry and Chemical Engineering, Chalmers University of Technology, 412 96 Gothenburg, Sweden; [orcid.org/0000-0002-1644-1965](https://orcid.org/0000-0002-1644-1965); Email: [jerker@chalmers.se](mailto:jerker@chalmers.se)

### Authors

**Steffen M. Brülls** – Department of Chemistry and Chemical Engineering, Chalmers University of Technology, 412 96 Gothenburg, Sweden; Present Address: Nouryon Surface Chemistry AB, Hamnvägen 2, 444 85 Stenungsund, Sweden

**Valentina Cantatore** – Department of Chemistry and Chemical Engineering, Chalmers University of Technology, 412 96 Gothenburg, Sweden; [orcid.org/0000-0003-2542-5550](https://orcid.org/0000-0003-2542-5550)

**Pui Lam Tam** – Department of Industrial and Materials Science, Chalmers University of Technology, 412 96 Gothenburg, Sweden

**Per Malmberg** – Department of Chemistry and Chemical Engineering, Chalmers University of Technology, 412 96 Gothenburg, Sweden; [orcid.org/0000-0002-6487-7851](https://orcid.org/0000-0002-6487-7851)

**Elisabet Ahlberg** – Department of Chemistry and Molecular Biology, University of Gothenburg, 412 96 Gothenburg, Sweden; [orcid.org/0000-0002-4946-4979](https://orcid.org/0000-0002-4946-4979)

**Itai Panas** – Department of Chemistry and Chemical Engineering, Chalmers University of Technology, 412 96 Gothenburg, Sweden

**Siegfried Eigler** – Institut für Chemie und Biochemie, Freie Universität Berlin, 14195 Berlin, Germany; [orcid.org/0000-0002-0536-8256](https://orcid.org/0000-0002-0536-8256)

Complete contact information is available at: <https://pubs.acs.org/doi/10.1021/acs.jpcc.2c07643>

### Author Contributions

The manuscript was written through contributions of all authors. S.B. prepared all compounds and 2D samples, as well as recorded Raman spectra and cyclic voltammograms. V.C. and I.P. performed DFT calculations. P.L.T. recorded the XPS spectra. P.M. recorded ToF-SIMS images. E.A. set up and analyzed the cyclic voltammetry experiments. S.E. originally proposed to explore the hexacation as a dopant. J.M. performed DFT calculations and coordinated the interpretation of experimental data and writing of the manuscript.

### Notes

The authors declare no competing financial interest.

## ■ ACKNOWLEDGMENTS

The Chalmers University of Technology Foundation is gratefully acknowledged for financial support. We thank the Chalmers Mass Spectrometry Infrastructure (CMSI) and the Swedish NMR Centre at the University of Gothenburg for their support with HR-MS and NMR measurements.

## ■ REFERENCES

- (1) Allen, M. J.; Tung, V. C.; Kaner, R. B. Honeycomb carbon: a review of graphene. *Chem. Rev.* **2010**, *110*, 132–145.
- (2) Novoselov, K. S.; Geim, A. K.; Morozov, S. V.; Jiang, D.; Zhang, Y.; Dubonos, S. V.; Grigorieva, I. V.; Firsov, A. A. Electric field effect in atomically thin carbon films. *Science* **2004**, *306*, 666–669.
- (3) Novoselov, K. S.; Jiang, D.; Schedin, F.; Booth, T. J.; Khotkevich, V. V.; Morozov, S. V.; Geim, A. K. Two-dimensional atomic crystals. *Proc. Natl. Acad. Sci. U. S. A.* **2005**, *102*, 10451–10453.
- (4) Bernal, J. D. The structure of graphite. *Proc. R. Soc. Lond., Ser. A* **1924**, *106*, 749–773.
- (5) Chung, D. D. L. Review graphite. *J. Mater. Sci.* **2002**, *37*, 1475–1489.
- (6) Liu, J. Q.; Tang, J. G.; Gooding, J. J. Strategies for chemical modification of graphene and applications of chemically modified graphene. *J. Mater. Chem.* **2012**, *22*, 12435–12452.
- (7) Dong, X. C.; Shi, Y. M.; Chen, P.; Ling, Q. D.; Huang, W. Aromatic molecules doping in single-layer graphene probed by Raman spectroscopy and electrostatic force microscopy. *Jpn. J. Appl. Phys.* **2010**, *49*, No. 01AH04.
- (8) Ferrari, A. C.; Basko, D. M. Raman spectroscopy as a versatile tool for studying the properties of graphene. *Nat. Nanotechnol.* **2013**, *8*, 235–246.
- (9) Zhan, J.; Lei, Z.; Zhang, Y. Non-covalent interactions of graphene surface: Mechanisms and applications. *Chem* **2021**, *8*, 947–979.
- (10) Björk, J.; Hanke, F.; Palma, C.-A.; Samori, P.; Cecchini, M.; Persson, M. Adsorption of aromatic and anti-aromatic systems on graphene through  $\pi$ - $\pi$  stacking. *J. Phys. Chem. Lett.* **2010**, *1*, 3407–3412.
- (11) Kolev, S. K.; Aleksandrov, H. A.; Atanasov, V. A.; Popov, V. N.; Milenov, T. I. Interaction of graphene with out-of-plane aromatic hydrocarbons. *J. Phys. Chem. C* **2019**, *123*, 21448–21456.
- (12) Kim, C. H.; Kymissis, I. Graphene-organic hybrid electronics. *J. Mater. Chem. C* **2017**, *5*, 4598–4613.
- (13) Zhang, Y.; Zhang, L.; Zhou, C. Review of chemical vapor deposition of graphene and related applications. *Acc. Chem. Res.* **2013**, *46*, 2329–2339.
- (14) Eigler, S.; Enzelberger-Heim, M.; Grimm, S.; Hofmann, P.; Kroener, W.; Geworski, A.; Dotzer, C.; Rockert, M.; Xiao, J.; Papp, C.; Lytken, O.; Steinruck, H. P.; Müller, P.; Hirsch, A. Wet chemical synthesis of graphene. *Adv. Mater.* **2013**, *25*, 3583–3587.
- (15) Eigler, S.; Hirsch, A. Chemistry with graphene and graphene oxide-challenges for synthetic chemists. *Angew. Chem., Int. Ed. Engl.* **2014**, *53*, 7720–7738.
- (16) Brülls, S. M.; Cantatore, V.; Wang, Z. P.; Tam, P. L.; Malmberg, P.; Stubbe, J.; Sarkar, B.; Panas, I.; Mårtensson, J.; Eigler, S. Evidence for electron transfer between graphene and non-covalently bound pi-Systems. *Chem. – Eur. J.* **2020**, *26*, 6694–6702.
- (17) Al Kurdi, K.; Gregory, S. A.; Jhulki, S.; Conte, M.; Barlow, S.; Yee, S. K.; Marder, S. R. Electron transport in a sequentially doped naphthalene diimide polymer. *Mater. Adv.* **2020**, *1*, 1829–1834.
- (18) Un, H. I.; Gregory, S. A.; Mohapatra, S. K.; Xiong, M.; Longhi, E.; Lu, Y.; Rigin, S.; Jhulki, S.; Yang, C. Y.; Timofeeva, T. V.; Wang, J. Y.; Yee, S. K.; Barlow, S.; Marder, S. R.; Pei, J. Understanding the effects of molecular dopant on n-type organic thermoelectric properties. *Adv. Energy Mater.* **2019**, *9*, No. 1900817.
- (19) Perdew, J. P.; Burke, K.; Ernzerhof, M. Generalized gradient approximation made simple. *Phys. Rev. Lett.* **1996**, *77*, 3865–3868.
- (20) Feng, R. Q.; Li, L. L.; Li, B.; Li, J. H.; Peng, D.; Yu, Y. T.; Mu, Q. H.; Zhao, N.; Yu, X. Q.; Wang, Z. H. A small- molecule with a



large two-photon absorption cross-section serves as a membrane-permeable ribonucleic acid (RNA) probe for live cell imaging. *New J. Chem.* **2018**, *42*, 14325–14331.

(21) Nguyen, P. T.; Nguyen, H. T.; Pham, H. Q.; Kim, J.; Cordova, K. E.; Furukawa, H. Synthesis and selective CO<sub>2</sub> capture properties of a series of hexatopic linker-based metal-organic frameworks. *Inorg. Chem.* **2015**, *54*, 10065–10072.

(22) Zhai, J. H.; Wan, A.; Wu, W. B. A review on the structure of cold-compressed graphite phase. *Mod. Phys. Lett. B* **2015**, *29*, No. 1530011.

(23) Ilic, S.; Pandey Kadel, U.; Basdogan, Y.; Keith, J. A.; Glusac, K. D. Thermodynamic hydricities of biomimetic organic hydride donors. *J. Am. Chem. Soc.* **2018**, *140*, 4569–4579.

(24) Ludvik, J.; Pragst, F.; Volke, J. Electrochemical Generation of Triplet-States - Simplified estimation of triplet energies by electro-generated chemi-luminescence based on the anodic cleavage of dimeric dihydroheteroarenes. *J. Electroanal. Chem.* **1984**, *180*, 141–156.

(25) Savéant, J. M. Evidence for concerted pathways in ion-pairing coupled electron transfers. *J. Am. Chem. Soc.* **2008**, *130*, 4732–4741.

(26) Ferrari, A. C. Raman spectroscopy of graphene and graphite: Disorder, electron-phonon coupling, doping and nonadiabatic effects. *Solid State Commun.* **2007**, *143*, 47–57.

(27) Seah, M. P. A Review of the Analysis of surfaces and thin-films by AES and XPS. *Vacuum* **1984**, *34*, 463–478.

(28) Chua, C. K.; Pumera, M. Selective removal of hydroxyl groups from graphene oxide. *Chem. – Eur. J.* **2013**, *19*, 2005–2011.

(29) Okpalugo, T. I. T.; Papakonstantinou, P.; Murphy, H.; McLaughlin, J.; Brown, N. M. D. High resolution XPS characterization of chemical functionalised MWCNTs and SWCNTs. *Carbon* **2005**, *43*, 153–161.

(30) Moulder, J. F.; Strickle, W. F.; Sobol, P. E.; Bomben, K. D. *Handbook of X-Ray Photoelectron Spectroscopy*; Perkin-Elmer Corp.: Norwalk, 1995.

(31) Chang, Z. H.; Yan, H.; Tian, J.; Pan, H. Y.; Pu, H. T. The effect of electric field on the oxidative degradation of polybenzimidazole membranes using electro-Fenton test. *Polym. Degrad. Stabil.* **2017**, *138*, 98–105.

(32) Finsgar, M. The first X-ray photoelectron spectroscopy surface analysis of 4-methyl-2-phenyl-imidazole adsorbed on copper. *Anal. Methods* **2015**, *7*, 6496–6503.

(33) Clarke, C. J.; Maxwell-Hogg, S.; Smith, E. F.; Hawker, R. R.; Harper, J. B.; Licence, P. Resolving X-ray photoelectron spectra of ionic liquids with difference spectroscopy. *Phys. Chem. Chem. Phys.* **2018**, *21*, 114–123.

(34) Men, S.; Mitchell, D. S.; Lovelock, K. R.; Licence, P. X-ray photoelectron spectroscopy of pyridinium-based ionic liquids: comparison to imidazolium- and pyrrolidinium-based analogues. *ChemPhysChem* **2015**, *16*, 2211–2218.

(35) Morales-Ugarte, J. E.; Benayad, A.; Santini, C. C.; Bouchet, R. Electrochemical impedance spectroscopy and x-ray photoelectron spectroscopy study of lithium metal surface aging in imidazolium-based ionic liquid electrolytes performed at open-circuit voltage. *ACS Appl. Mater. Interfaces* **2019**, *11*, 21955–21964.

(36) Shi, G.; Chen, L.; Yang, Y.; Li, D.; Qian, Z.; Liang, S.; Yan, L.; Li, L. H.; Wu, M.; Fang, H. Two-dimensional Na-Cl crystals of unconventional stoichiometries on graphene surface from dilute solution at ambient conditions. *Nat. Chem.* **2018**, *10*, 776–779.

## Recommended by ACS

### Can Ag<sup>+</sup> Permeate through a Potassium Ion Channel? A Bottom-Up Approach by Infrared Spectroscopy of the Ag<sup>+</sup> Complex with the Partial Peptide of a Selectivity Filter

Satoru Tanabe, Masaaki Fujii, *et al.*

MARCH 16, 2023

THE JOURNAL OF PHYSICAL CHEMISTRY LETTERS

READ 

### Electrochemical, Scanning Electrochemical Microscopic, and In Situ Electrochemical Fourier Transform Infrared Studies of CO<sub>2</sub> Reduction at Porous Copper Surfaces

Allison Salverda, Aicheng Chen, *et al.*

APRIL 05, 2023

THE JOURNAL OF PHYSICAL CHEMISTRY C

READ 

### Nonpolymer Organic Solar Cells: Microscopic Phonon Control to Suppress Nonradiative Voltage Loss via Charge-Separated State

Takaaki Nagatomo, Yasuhiro Kobori, *et al.*

DECEMBER 30, 2022

ACS PHYSICAL CHEMISTRY AU

READ 

### Molecular-Engineered Biradicals Based on the Y<sup>III</sup>-Phthalocyanine Platform

Nithin Suryadevara, Mario Ruben, *et al.*

JANUARY 19, 2023

JOURNAL OF THE AMERICAN CHEMICAL SOCIETY

READ 

Get More Suggestions >